Improved Solid Electrolyte Conductivity via Macromolecular Self-Assembly: From Linear to Star Comb-like P(S- co -BzMA)- b -POEGA Block Copolymers

Kingsley Ikenna Aniagbaoso, Monika Król, Janne Ruokolainen, Antoine Bousquet, Maud Save, Laurent Rubatat

Improved Solid Electrolyte Conductivity via Macromolecular Self-Assembly: From Linear to Star Comb-like P(S-*co*-BzMA)-*b*-POEGA Block Copolymer

Kingsley Ikenna Aniagbaoso,[1] Monika Król,[2] Janne Ruokolainen,[2] Antoine Bousquet,[1] Maud Save,[1] Laurent Rubatat[1*]

[1] *Universite de Pau et des Pays de l'Adour, E2S UPPA, CNRS, IPREM, Pau, France*

[2] *Department of Applied Physics, School of Science, Aalto University, Espoo FIN-00076, Finland*

* Corresponding author: laurent.rubatat@univ-pau.fr

Abstract

Star block copolymer electrolyte with lithium ion conducting phase are investigated in the present work to assess the influence of this complex architecture compared to the linear one, on both, bulk morphology and ionic conductivity. For that purpose, the controlled synthesis of a series of poly(styrene-*co*-benzyl methacrylate)-*b*-poly[oligo(ethylene glycol) methyl ether acrylate] (P(S-*co*-BzMA)-*b*-POEGA) block copolymers (BCPs) by RAFT polymerization was performed from either a monofunctional or a tetrafunctional chain transfer agent (CTA) containing trithiocarbonate groups. We emphasized how a small amount of styrene (6 mol-%) improved drastically the control of the RAFT polymerization of benzyl methacrylate mediated by the tetrafunctional CTA. Transmission electron microscopy (TEM) and small angle X-ray scattering (SAXS) demonstrated a clear segregation of the BCPs in the presence of lithium salt. Interestingly, the star BCPs gave rise to highly ordered lamellar structures compared to the linear analogue. Consequently, the reduced lamellae tortuosity of self-assembled star BCPs improved the lithium conductivity by more than 8 times at 30°C for~30 wt-% of POEGA conductive phase.

Keywords: Battery; Solid polymer electrolyte; Block copolymers; Star architecture; Self-assembly

INTRODUCTION

Lithium ion batteries have gained increasing interest over the years as mobile energy storage for electric vehicles (EVs), personal electronic devices, etc.[1] Development of low cost, high energy density and safe batteries have been the core of many research endeavours since the last three decades.

Indeed, organic solvent based liquid electrolytes, classically used in commercialized lithium ion batteries, constitute a hazard due to leakage and flammability. To tackle that issue, solid polymer electrolytes (SPEs) with tunable mechanical properties are considered.[2] The most commonly investigated polymer is the low glass transition temperature (T_g) and semi-crystalline poly(ethylene oxide) (PEO).[3] However, its lithium ion conductivity remains low compared to liquid electrolytes. Improved ion transport can be achieved at temperatures above melting temperature, activated by an increased macromolecular segmental motion[4] and a reduced crystallinity.[5] Lower PEO crystallinity can be realized at room temperature by breaking up the long-range macromolecular symmetry. This can be achieved by either utilizing PEO with comb or star macromolecular architectures or incorporating inorganic nanoparticles.[5-7] Comb-like architecture can be obtained by polymerization of oligo(ethylene glycol (meth)acrylate) (OEGA or OEGMA) macromonomer to provide polymer backbone grafted with short pendant ethylene oxide (EO) oligomers.[8] Star-shaped PEO has also demonstrated a reduced degree of crystallinity and melting temperature (T_m) compared to the linear PEO.[6] That is resulting from the globular structure in a star-shaped polymer which hinders arm packing for crystallization.[9] Nevertheless, the loss of crystallinity induces a loss of mechanical properties. In this context, the use of block copolymer electrolyte (BCPE) has been considered in order to achieve a compromise between mechanical and ion transport properties.[10] Indeed, BCPEs containing at least one Li^+-conductive polymer block and one high-T_g block are expected to simultaneously exhibit good levels of ionic conductivity and mechanical strength. Major studies throughout the years focused on linear BCPE systems based on PEO, especially the polystyrene-*block*-poly(ethylene oxide) (PS-*b*-PEO) copolymers where ionic conductivity, mechanical properties and microphase separation have been extensively studied.[11-18] Devaux *et al.* showed that lowering both melting temperature (T_m) and degree of crystallinity via the comb-like architecture of POEGMA-*b*-PS block copolymer improve lithium conductivity compared to the linear PEO-*b*-PS.[19] The influence of side chain length and graft density was studied by Butzelaar *et al.*. [20] They demonstrated for a library of polymers featuring different PEO side-chain lengths a drastic reduction in PEO crystallinity by 98% for 11 side EO units and by 39% for 54 side EO units in comparison to pure PEO.[20] Regarding the high-T_g block, PS is largely used but other high-T_g blocks have been studied. For instance, BCP of poly(methyl methacrylate) (PMMA) and POEGMA were reported by Ruzette *et al.* where they demonstrated that microphase separation can be induced in a controlled manner by the incorporation of lithium salt.[21] Such BCPEs showed higher conductivity than the statistical analogue copolymers.[21] Later, triblock copolymer based on poly(benzyl methacrylate) (PBzMA) and POEGMA (EO = 9) were synthesized as BCPE; this study also revealed that the phase separation of BCP is triggered by the addition of lithium bis(trifluoromethane)-sulfonylimide (LiTFSI) salt.[22]

Star BCP have attracted increasing attention in various applications due to the compact and stabilizing steric structure, which may lead to peculiar morphological and rheological properties.[23-24] Few reports have described the use of star BCP as solid electrolytes in lithium ion batteries,[25-29] but only two studies have compared the performances with their linear analogues in details. In the first study, a miktoarm BCPE consisting of 3-arms PEO connected to a PS block was shown to promote long-range narrow lamellar morphologies with high conductivities whereas the linear analogue showed swirly broader lamellar morphology with lower ionic conductivities.[25] In the other study, six-arm star PS-*b*-POEGMA BCP with a discotic liquid crystal core reportedly exhibit longer range ordered morphology and ionic conductivity 8 times higher than that of the corresponding linear BCPE; however, the presence of the discotic liquid crystal core in the star copolymer hinders an accurate comparison.[26]

The interest of the present work is to combine star architecture with comb-like character of POEGA in order to investigate the effect of such architecture on morphology and lithium ion conductivity of the self-assembled BCPEs. For that purpose, we first undertook the synthesis of linear and star high-T_g first block by reversible addition fragmentation transfer (RAFT) polymerization via a core-first approach (Scheme 1). Two different chain transfer agents (CTA), either monofunctional or tetrafunctional, were used to copolymerize benzyl methacrylate (BzMA) with increasing fraction of styrene (S) to achieve the best control of polymerization. The second block of poly(oligo(ethylene glycol) methyl ether acrylate) (POEGA) was then synthesized by chain extension of the linear or star P(S-*co*-BzMA) macromolecular chain transfer agent (macroCTA) to produce the desired BCPs. Finally, solid electrolytes were prepared by mixing the BCPs with lithium bis(trifluoromethanesulfonyl)imide (LiTFSI) salt to investigate their morphology by SAXS and TEM in relationship with their ionic conductivity.

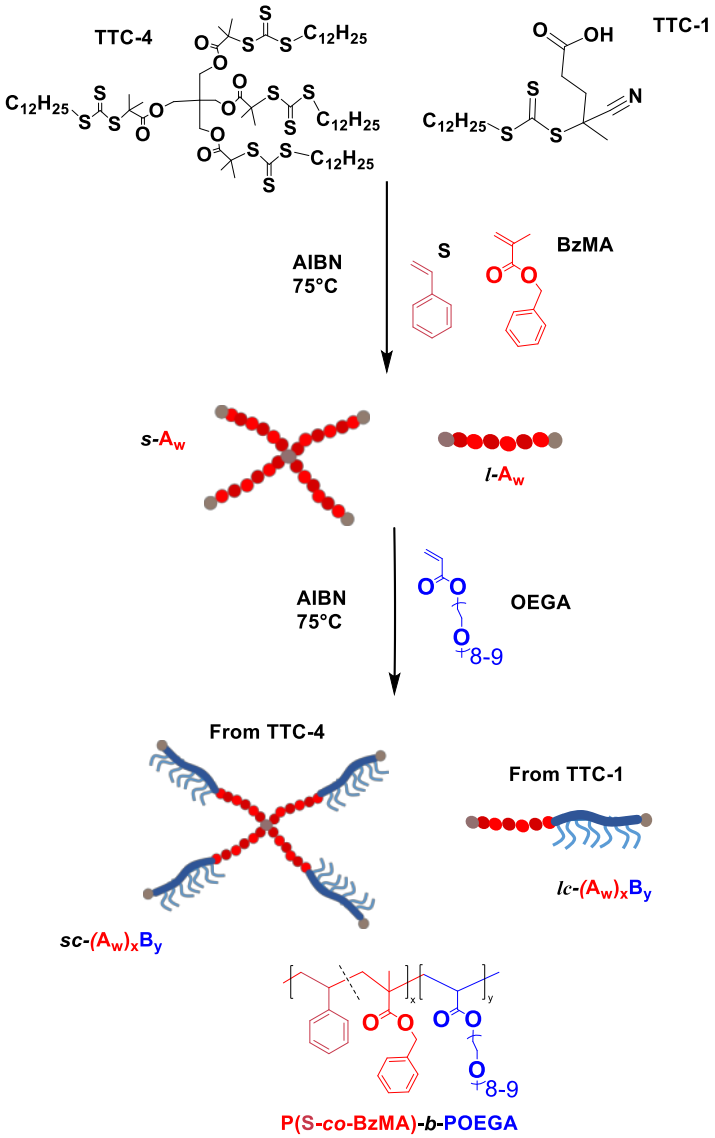

Scheme 1. Schematic illustration of the synthesis route to synthesize *lc*-$(A_w)_xB_y$ and *sc*-$(A_w)_xB_y$ block copolymers (BCP) by RAFT polymerization using either TTC-1 monofunctional CTA or TTC-4 tetrafunctional CTA. The A block corresponds to the P(S-*co*-BzMA) block and B block to POEGA. The subscripts *w* represents the weight fraction of the BzMA compared to S in the macro-CTA, the subscripts *x* and *y* correspond respectively to the weight fractions of P(S-*co*-BzMA) hard block and POEGA soft block in the AB block copolymer. The prefix *lc*- and *sc*- depicts the linear comb-like or star comb-like architecture.

EXPERIMENTAL PART

Materials

Benzyl Methacrylate (BzMA, Sigma-Aldrich, 96%) was passed through a silica gel column to remove monomethyl ether hydroquinone inhibitor. Styrene (S, Sigma-Aldrich, 99%$^+$), Azobis(isobutyronitrile) (AIBN, Sigma-Aldrich, 98%), Oligo(ethylene glycol) methyl ether acrylate

(OEGA, DPn = 8-9, average M_n = 480 g.mol^{-1}, Sigma-Aldrich) were used as purchased. Pentaerythritol tetrakis[2-(dodecylthiocarbonothioylthio)-2-methylpropionate (tetrafunctional chain transfer agent named TTC-4, Sigma-Aldrich, 97%), 4-cyano 4-[(dodecylsulfanylthiocarbonyl)-sulfanyl]-pentanoic acid (monofunctional chain transfer agent named TTC-1, Sigma-Aldrich, 97%), Lithium bis(trifluoromethanesulfonyl)imide (LiTFSI, Sigma-Aldrich, 99%$^+$ anhydrous), Tetrahydrofuran (THF, Sigma-Aldrich, 99%$^+$), Ethanol (EtOH, VWR, 96%$^+$), linear PS standards (Polymer Standards Service GmbH).

Synthesis of linear and star macro-CTA of P(S-*co*-BzMA)

Polymerizations were performed with a total of 8 g of monomers, varying the initial molar fractions of BzMA and S from $f_{BzMA,0}$ = 0 to 1 as described in Table 1. In a typical experiment, *s*-$A_{0.62}$ for synthesis of star macro-CTA, AIBN (2.5 mg, 1.63 10^{-2} mmol, 0.1 eq), TTC-4 (61.0 mg, 4.07 × 10^{-2} mmol TTC-4 = 1.63 × 10^{-1} mmol of trithiocarbonate TTC function, 1 eq), BzMA (4.00 g, 2.27 ×10^{-2} mol, 139 eq), and S (4.00 g, 3.85 × 10^{-2} mol, 236 eq) were mixed in a 25 mL round bottom flask and sealed with a septum. The reactant mixture was degassed with nitrogen bubbling for 20 min in an ice bath. A sample was withdrawn under nitrogen at time t = 0 for kinetic. The round bottom flask was placed into an oil bath at previously heated to 75 °C to start the reaction. Kinetic samples were collected at regular intervals under nitrogen flow for nuclear magnetic resonance (NMR) and size exclusion chromatography (SEC) analysis. The reaction was stopped at t = 31.5 h by cooling down in an ice -water bath and by introduction of oxygen in the crude mixture. Purification was done by addition of 2 vol. equivalence of THF to solubilize the crude mixture and precipitation into 10 vol. equivalence of EtOH at room temperature. Purification was performed twice to ensure complete removal of unreacted monomer and precipitated polymers were recovered via vacuum filtration and dried under vacuum for 72 h. Individual conversions of monomers (x_{BzMA} and x_S) were calculated from ^{1}H NMR spectra (see Eq S1, Eq S2 and Figure S1). The equations for the calculation of the overall molar (X_m) and weight (X_w) conversion in both S and BzMA monomers are detailed in Supporting Information along with the calculations of the fractions of BzMA units in the P(S-*co*-BzMA) copolymer.

Synthesis of linear comb-like and star comb-like P(S-*co*-BzMA)-*b*-POEGA block copolymer

MacroCTA of P(S-*co*-BzMA) previously synthesized were used for the bulk RAFT polymerization of OEGA using AIBN as initiator (Table 2). In a typical experiment *sc*-$(A_{0.62})_{0.80}B_{0.20}$, AIBN (0.9 mg, 5.57 ×$10^{-3}$ mmol), *s*-$A_{0.62}$ macroCTA (1.7 g, M_n = 122 kg.mol^{-1}, 1.39 ×10^{-2} mmol = 5.57 ×10^{-2} mmol TTC), and OEGA (10.2 g, 21.3 mmol) were inserted in a 25 mL round bottom flask and sealed with a septum. The reactant mixture was left to stand for 50 min under stirring conditions. In the case of

PS macroCTA, the polymerization was performed in a solution mixture of OEGA and 1,4-dioxane (1/1, v/v) due to insolubility of PS in OEGA. The reaction mixture was degassed with nitrogen bubbling for 30 min in an ice bath. A sample was withdrawn under nitrogen at time $t = 0$. The round bottom flask was placed into an oil bath at previously heated 75 °C to start the reaction. The reaction was stopped at $t = 50$ min for *sc*-$(A_{0.62})_{0.80}B_{0.20}$ (or up to 2 h for *sc*-$(A_{0.62})_{0.23}B_{0.77}$) by cooling down in an ice-water bath and by introduction of oxygen in the crude mixture. Note that synthesis of *sc*-$(A_{0.62})_{0.73}B_{0.27}$ was performed with 50 vol-% of 1,4-Dioxane based on OEGA to enable the decrease of the initial OEGA content while enabling solubilisation of macroCTA. Purification was done by addition of 5 vol. equivalence of THF to solubilize the crude mixture and dialyzed over distilled water using 50kDa regenerated cellulose membrane. Dialysis was carried out over 6-water cycles to ensure complete removal of unreacted OEGA monomer and dialyzed sample is lyophilized. Conversion of OEGA was determined from Eq S18 by taking the integral of one aromatic proton (7.5 – 6.4 ppm) of P(BzMA-*co*-S) first block as internal standard.

Preparation of Block Copolymer Electrolytes (BCPEs) films. Electrolyte solutions were prepared by mixing as prepared BCPs with an equivalent amount of LiTFSI salt ([EO]/[Li] = 15) in THF (0.39 g/mL). Polymer electrolyte films for conductivity, TEM and X-ray scattering were made by solvent-casting the electrolyte solution onto a stainless-steel disc. Samples were allowed to dry in the vacuum oven for 24 h. Thereafter, the samples could be peeled off as free-standing films (see Figure S16) with typical thickness range, $L \approx 90 – 470$ μm. The volume fraction of conducting phase, ϕ_c, was estimated from Eq S21 by using the densities of POEGA homopolymer (1.54 g cm^{-3}), PS (1.05 g cm^{-3}), PBzMA (1.17 g cm^{-3}) and LiTFSI (1.33 g cm^{-3}).[30] The density of the BCP was calculated using Eq S22. The density of the POEGA homopolymer was estimated using Van Krevelen's method, and the details of this calculation are shown in Table S5.[31] The resulting values of ϕ_c are given in Table S4.

Characterization Methods

Nuclear Magnetic Resonance (NMR) Spectroscopy. NMR spectra were recorded using a Bruker 400 MHz spectrometer at 25 °C with 32 scans and a time delay D1 of 5 seconds. ^{1}H NMR measurements were performed at frequencies of 400 MHz. DOSY NMR spectra were recorded at 30 °C with 6000 scans and a time delay D1 of 2 seconds. Deuterated chloroform ($CDCl_3$) and deuterated dichloromethane (CD_2Cl_2) were used as solvent respectively for crude and purified polymer. All products were dissolved with concentrations between 10 and 20 mg/mL.

Size Exclusion Chromatography – Multi-Angle Laser Light Scattering (SEC-MALLS). Measurements were performed on a bank of 4 Shodex columns (KF801, KF8025, KF804 and KF806) each 300 mm x 8 mm at 30 °C with THF eluent controlled by a Malvern pump (Viscotek, VE1122) at a flow rate of 1.0 mL.min^{-1}. The SEC apparatus is equipped with a refractive index (RI) detector (Viscotek VE3580), a Wyatt Heleos II Multi Angle Laser Light Scattering detector (MALLS, 18 angles, λ_0 = 664.4 nm), an online viscometer (Wyatt Viscostar 311-V4) and a UV-visible detector (Viscotek-Malvern VE3210). Toluene was used as a flow marker. Sample concentrations were limited to the range of 1.5 – 4.5 mg mL^{-1} and dissolved samples were filtered through polytetrafluorethylene (PTFE) membranes with a pore size of 0.45 μm prior to injection. The refractive index increments (dn/dc) of each polymer for MALLS analysis are reported in Table S1 and S2

Differential Scanning Calorimetry (DSC). DSC was performed using the Q100 from TA instruments under a N_2 atmosphere. For each sample, the temperature regime was initially stabilized at -80 °C for 5 min, heating and cooling was done within -80 and 120 °C with a rate of 5 °C.min^{-1}. The heat capacity change in the second heating scan was used for the determination of the glass transition temperature (T_g).

Electrochemical Impedance Spectroscopy (EIS). Free-standing BCPE films were previously dried in the vacuum oven for 24 h and stored in the glove box (see Figure S16). The films (8 mm ø, thickness, L ≈ 90 – 470 μm) were sandwiched between two blocking gold electrodes plates in CESH-e (Enhanced Controlled Environment Sample Holder) cells (ø 6.35 mm) and EIS measurement using Biologic Potentiostat (equipped with EC-Lab software package) at frequency from 1 Hz to 1 MHz with an oscillating voltage of 50 mV. Subsequently, these cells were preconditioned in a temperature chamber (Binder KB53, 230V 1~ 50Hz) for 2 h at 90 °C to anneal the films. After the preconditioning was finished, measurements were carried out by gradually decreasing the temperature in 20 °C steps from 90 °C to -10 °C with each temperature being maintained for 2 h to attain a thermal equilibrium. The ionic conductivity (σ; S cm^{-1}) was determined by $\sigma = L/RA$ where R is the measured resistance, L is the film thickness and A is the area of the electrode.

Small Angle X-ray Scattering (SAXS). Small angle X-ray scattering SAXS measurement was performed on Xenoxs Xeuss 3.0 equipped in Cu Kα radiation source (λ = 1.54 Å) and Eiger2 R 1M by Dectris 2D detector. The sample to detector distance was 1.1 m. Pristine samples were sealed in the heating stage between two Kapton foils. The scattering data was collected at chosen temperature points during heating/cooling cycle (25, 100, 90, 70, 50, and 30 °C) under vacuum in order to track any possible temperature induced changes in self-assembly. Films were heated/cooled down with rate

5 °C/min. Virtual detector mode was used, acquiring three images in horizontal plane (240 s exposure time for each). Each temperature point was measured twice after maintaining for 1 h to attain a thermal equilibrium. Data was subjected to standardized correction including background subtraction and azimuthal averaging of the 2D scattering data to obtain 1D SAXS profiles. Temperature dependent scattering curves were plotted as a function of scattering vector q; its magnitude is given by $q = 4\pi \sin\theta/\lambda$, where 2θ is the scattering angle.

Transmission Electron Microscopy (TEM). Ultra-thin sections (~70 nm) for TEM characterization was prepared from previously solvent casted BCPE films. Samples were annealed at 100 °C for approximately 1 h. Subsequently, samples were fixed to a pin and cut at – 80 °C with Diatome 25 ° diamond knife on a Leica EM UC7 cryo-ultramicrotome. Sections were collected and transferred on 300 mesh copper grid coated with lacey carbon. Prepared grids were immersed in liquid nitrogen and cryo-transferred to microscope in order to prevent moisture accumulation. CryoTEM measurements were performed on Schottky field-emission cryo-electron microscope JEOL JEM-3200FSC at 300 kV accelerating voltage, while keeping the temperature of the examined specimen at – 187 °C. The micrographs were acquired in bright field mode using zero energy loss omega type filter with a slit width 20 eV and with slight under focus. Images were recorded via Gatan Ultrascan 4000 CCD camera.

RESULTS AND DISCUSSION

RAFT copolymerization of Styrene and Benzyl Methacrylate. In the present work, RAFT polymerization of benzyl methacrylate (BzMA) was first carried out via two different chain transfer agents (CTA), either the monofunctional trithiocarbonate (TTC-1) or the tetrafunctional trithiocarbonate (TTC-4) in order to produce linear or star polymers (Scheme 1). Both CTA are non-symmetrical trithiocarbonate exhibiting identical stabilizing Z-group ($-CH_2(CH_2)_{10}CH_3$) but different R-initiating groups (Scheme 1). The tetrafunctional CTA contains the R group in the core to preserve the star architecture whatever the degree of livingness (Scheme 1). The polymerization was performed in bulk with constant initial [CTA]/[AIBN] ratio and constant value of AIBN concentration across all synthesis (Table 1). Number-average molar mass (M_n) and dispersity ($Đ$) of samples taken during polymerization were determined using SEC-MALLS and plotted as a function of the overall weight monomer conversion (Figure 1). By using the TTC-1 monofunctional CTA, a linear evolution of M_n versus conversion is observed on Figure 1(left), for BzMA homopolymerization but the values are slightly higher compared to theoretical ones ($M_{n,SEC\text{-}MALLS}/ M_{n,theo} \sim 1.15$ for PBzMA). Such

discrepancy between experimental and theoretical M_n is even more pronounced on Figure 1(right) when RAFT polymerization is carried out with the TTC-4 tetrafunctional CTA ($M_{n,SEC\text{-}MALLS}$/ $M_{n,theo}$ ~ 1.57 for PBzMA), along with higher dispersity values. This cannot be ascribed to bias in SEC measurement as M_n were determined by MALLS and not relative to any standard calibration. As previously reported in the literature, this trend is characteristic of a low chain transfer constant ($C_{tr} = k_{ex}/k_p$) in RAFT polymerization.[32] The leaving R group plays a role on the exchange rate and especially the fragmentation step. Note that both CTAs display two different R groups: (C(CN)(CH$_3$)CH$_2$CH$_2$COOH) for TTC-1 monofunctional CTA and (-C(CH$_3$)$_2$CO$_2$CH$_2$-) for TTC-4 tetrafunctional CTA. Based on profiles reported in reference [32], one can conclude from Figure 1 that BzMA RAFT polymerization mediated with TTC-1 is associated with C_{tr} above 1 while C_{tr} is probably far below 1 for TTC-4.

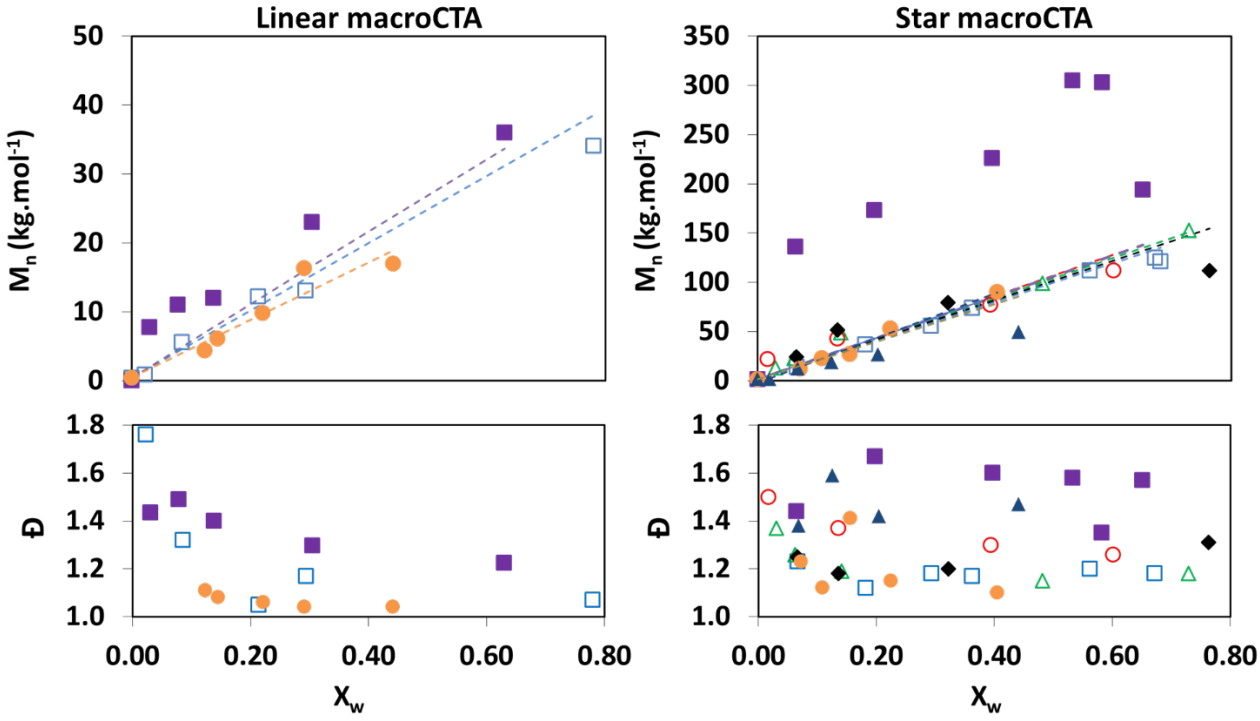

Figure 1. Evolution of $M_{n,MALLS}$ and dispersity of P(S-co-BzMA) copolymers versus the overall monomer weight conversion (X_w, see Eq S4) for various initial molar fractions in BzMA: ● $f_{BzMA,0}$ =0, ▲ $f_{BzMA,0}$ =0.19, □ $f_{BzMA,0}$ =0.38, ◆ $f_{BzMA,0}$ =0.50, Δ $f_{BzMA,0}$ =0.75, ○ $f_{BzMA,0}$ =0.94, ■ $f_{BzMA,0}$ =1. (Left) Theoretical trends (eq S14) are represented with dotted lines.

In order to favor fragmentation of the initial CTA, we decided to introduce styrene as comonomer since styrenic monomers are less stabilized compared to the *R*-group of TTC-4. Monomer feed molar composition was varied from 1 to 0 in BzMA to synthesize a series of P(S-*co*-BzMA) statistical copolymers and PS homopolymer from both TTC-1 and TTC-4 CTAs. Table 1 shows a summary of

the compositions of the initial monomer feed ($f_{BzMA,0}$) and of final purified copolymer (F_{BzMA}) together with values of molar mass and dispersity of the copolymers. Figure 1 shows that by adding as little as 6 mol% of styrene in the feed monomer composition (f_{BzMA} = 0.94), the experimental $M_{n,SEC\text{-}MALLS}$ values of star copolymers match perfectly with theoretical values and dispersity values are reduced to 1.3.Thus, the introduction of low fraction of styrene induces an increase of C_{tr} value, thus enabling to control the synthesis of star copolymers based on PBzMA. It should be noted that the M_n values of the series of P(S-*co*-BzMA) copolymers and PS homopolymer perfectly match the theoretical M_n values by using both monofunctional and tetrafunctional CTAs (Figure 1 left). The SEC chromatograms depicted in Figure S2 show monomodal traces for linear and star P(S-*co*-BzMA) copolymers synthesized at different monomer feed ratios ($f_{BzMA,0}$ from 1 to 0.38), as well as for linear PBzMA homopolymer. The shift of SEC traces towards lower elution volume upon increasing monomer conversion together with linear evolution of M_n confirms control of RAFT polymerization. On the other hand, the lower shift of SEC traces of star PBzMA (Figure S2) is in accordance with low C_{tr} value of the tetrafunctional CTA towards methacrylate monomers, as discussed above.

Table 1. Final Composition and Macromolecular Features of the P(S-*co*-BzMA) macro-CTA Synthesized by RAFT Copolymerization in Bulk

CTA	$f_{BzMA,0}$[a]	$[M]_0$:$[TTC]_0$ [b]	t (h)	X_w[c] (%)	W_{BzMA}[d]	$M_{n,theo}$[e] (kg.mol^{-1})	$M_{n,MALLS}$[f] (kg.mol^{-1})	$Đ_{MALLS}$	macro-CTA[g]
TTTC-4	1.00	300:1	3.0	65	1.00	138	217	1.51	***s*-A$_{1.0}$**
	0.94	300:1	3.0	60	0.98	128	123	1.25	***s*-A$_{0.98}$**
	0.74	325:1	7.5	73	0.86	151	152	1.15	***s*-A$_{0.86}$**
	0.51	350:1	22	76	0.71	155	134	1.25	***s*-A$_{0.71}$**
	0.38	375:1	31.5	68	0.62	135	122	1.30	***s*-A$_{0.62}$**
	0.21	350:1	49.0	57	0.43	113	80	1.39	***s*-A$_{0.43}$**
	0	500:1	96.0	52	0	110	122	1.20	***s*-A$_0$**
TTC-1	1.00	300:1	3	62	1.00	33	38	1.10	***l*-A$_{1.0}$**
	0.38	300:1	27	76	0.59	31	28	1.06	***l*-A$_{0.59}$**
	0	440:1	95	52	0	25	22	1.04	***l*-A$_0$**

[a] $f_{BzMA,0}$ is the molar fraction of BzMA in the initial monomer feed (See Eq. S5 in SI).
[b] $[TTC]_0$ is the concentration in trithiocarbonate functions, $[TTC]_0 = [TTC\text{-}1]_0 = 4 \times [TTC\text{-}4]_0$ and $[M]_0 = [S+BzMA]_0$. $[AIBN]_0$=1.98 mmol.L^{-1}, $[TTC]_0$ /$[AIBN]_0$ =10.
[c] Overall weight conversion of both S and BzMA monomers (Eq S4 in SI).
[d] W_{BzMA} (See Eq S11 in SI) is the weight fraction of BzMA in the copolymer after purification determined from $F_{BzMA,\gamma}$ molar fraction measured by ^{1}H NMR (See Eq. S10 in SI).

[e] $M_{n,theo}$ is calculated from Eq. S13 in SI
[f] M_n values obtained from the SEC analysis with RI/MALLS detectors (see determination of dn/dc values for each copolymer in Table S1 and Table S2)
[g] *s*- and *l*- represents the star and linear P(S-*co*-BzMA) copolymers respectively, and the subscript is the weight fraction of BzMA (W_{BzMA}) in the purified macroCTA.

The semilogarithmic kinetic plot of the overall monomer conversion versus time is linear for each monomer feed composition (Figure 2) and for both mono and tetrafunctional CTAs. This means that there is a constant number of propagating radicals in the systems. As the fraction of BzMA in monomer feed ($f_{BzMA,0}$) decreases, the apparent average rate constant of copolymerization ($<k_p>[P^\bullet]$) is significantly decreased. The value of the average rate constant of copolymerization ($<k_p>$) depends on two criteria:[33] values of reactivity ratios and values of individual rate constant of homopolymerization (k_p (S) = 87 L mol^{-1} s^{-1} and (k_p (BzMA) = 390 L mol^{-1} s^{-1} at 25°C according to reference (see Figure S3).[34]

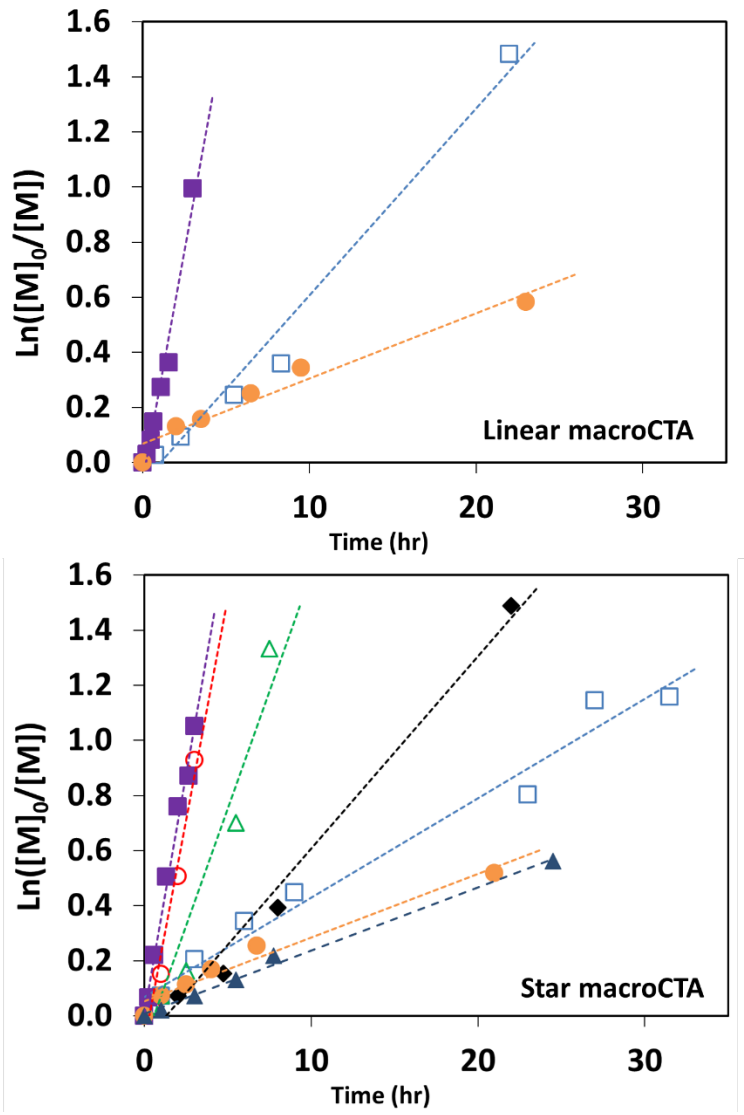

Figure 2. Semi-logarithmic plots of overall molar monomer conversion (X_m) versus time for RAFT copolymerization of S and BzMA from either TTC-1 (top) or TTC-4 (bottom) CTA at different monomer feed ratios (Table 1): ● $f_{BzMA,0}$ =0, ▲ $f_{BzMA,0}$ =0.2, □ $f_{BzMA,0}$ =0.38, ◆ $f_{BzMA,0}$ =0.50, Δ $f_{BzMA,0}$ =0.75, ○ $f_{BzMA,0}$ =0.94, ■ $f_{BzMA,0}$ =1. Dotted lines are linear fits.

Two sets of values for reactivity ratio of styrene and BzMA are reported in the literature: r_S = 0.46 ± 0.02, r_{BzMA} = 0.52 ± 0.08,[35] and r_S = 0.27 ± 0.14, r_{BzMA} = 0.86 ± 0.36 for nitroxide-mediated polymerization (NMP).[36] In the present work, we determined reactivity ratio of S/BzMA with extended Kelen-Tüdos (e-KT) method (see Figure S5 and equations in supporting information). We considered the composition of the purified copolymers ($F_{BzMA,\gamma}$, Eq S11) which was measured by ^{1}H NMR in CD_2Cl_2 for better accuracy compared to measurements in $CDCl_3$ as signal of $CHCl_3$ overlaps with aromatic protons (Table S1). Data of Figure S5 provided values of reactivity ratios of r_S = 0.70 ± 0.20 and r_{BzMA} = 0.67 ± 0.09. In order to assess the distribution of comonomer along the polymer chain of macroCTA, the experimental fraction in BzMA in the monomer feed (f_{BzMA}, Eq S6) was

monitored with time and plotted over the overall molar monomer conversion (X_m, Eq S3) (Figure 3). Such data could be fitted with Skeist equation as another method of determination of the reactivity ratios but in the present case the number of experimental points was too low for an accurate fitting. Figure 3 shows a quasi-constant fraction of BzMA comonomer during RAFT copolymerization in the absence of significant drift in monomer composition at least for monomer conversion below 80 % applied in the present work. As polymer chains are supposed to grow simultaneously in RAFT polymerization for sufficiently high value of C_{tr}, the homogeneous distribution of both monomers along the copolymer chain is expected to be similar for all chains. In addition, it is interesting to note that the plots of theoretical f_{BzMA} (dotted lines in Figure 3), calculated from reactivity ratios determined by the extended Kelen-Tüdos method in the present work (r_S = 0.70 ± 0.20 and r_{BzMA} = 0.67 ± 0.09), fit well with experimental data. On the other hand, a higher deviation between fitted plots and experimental data is observed for f_{BzMA} below 0.5 when applying values of reactivity ratio of r_S = 0.27 ± 0.14, r_{BzMA} = 0.86 ± 0.36 from literature [36] (see Figure S4).

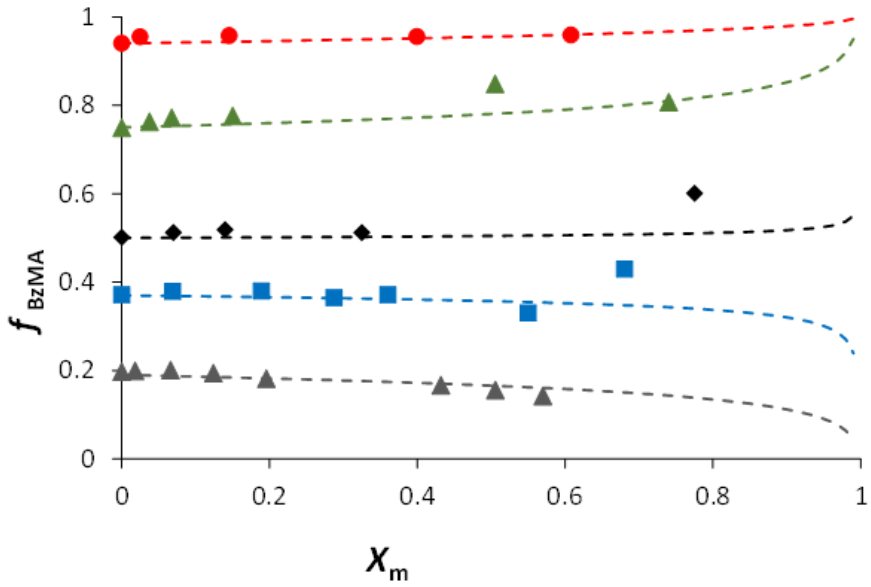

Figure 3. Evolution of BzMA fraction in monomer feed with X_m conversion. ▲ $f_{BzMA,0}$ = 0.19, ■ $f_{BzMA,0}$ = 0.38, ◆ $f_{BzMA,0}$ = 0.50, ▲ $f_{BzMA,0}$ = 0.75, ● $f_{BzMA,0}$ = 0.94. The dotted line corresponds to the fit of f_{BzMA} versus conversion calculated from Eq S8 by using reactivity ratios of present work (r_S = 0.70 ± 0.20 and r_{BzMA} = 0.66 ± 0.09).

In order to confirm the synthesis of statistical copolymers, the T_g evolution of the star macroCTAs *vs.* $f_{BzMA,0}$ was investigated by DSC. The series of P(BzMA-*co*-S) copolymers (Figure S6) exhibited indeed a single glass transition temperature (T_g) peak appearing between T_g values of both homopolymers ($T_{g,PBzMA}$ = 58°C, $T_{g,PS}$ = 100°C). The T_g increased with decreasing weight fraction of BzMA (W_{BzMA}) in agreement with theoretical ($T_{g,theo}$) calculations from the Fox-Flory equation (Eq S17, see Figure S7) as expected for statistical copolymers.

Characterization of star architecture.

The number of arms, *f*, for star polymers with monodispersed arm length can be determined from the contraction factor, *g*, defined in Eq 1 and Eq 2.[37]

$$g = \frac{3f - 2}{f^2} \quad (1)$$

$$g = \left[\left(\frac{[\eta]_s}{[\eta]_l}\right)_M\right]^{1/\varepsilon} \quad (2)$$

$[\eta]_s$ and $[\eta]_l$ represents the intrinsic viscosities of the star and linear polymer respectively, at the same molar mass M, and ε is known as the viscosity shielding ratio which describes the draining behaviour of the polymer in solution.[38] The ε value were reported to generally fall in the range of 0.5 to 1.5.[37] The branched structure of star PS synthesized by RAFT polymerization from TTC-4 CTA (*s*-A_0 in Table 1) was assessed from the determination of the contraction factor by comparison with linear standard PS samples (see experimental part). Kinetic samples taken at different intervals during synthesis of the star PS were analysed by SEC with an online viscosimeter. The logarithmic plot of intrinsic viscosity against molar mass (Log [η] vs Log M) were plotted for each chromatogram (see Figure S8). The linear regression of the experimental values provided an average value of the Mark-Houwink-Sakurada exponent ($[\eta] = KM^{\alpha}$) equal to $\alpha_{s\text{-}PS} = 0.58$ for star PS and $\alpha_{l\text{-}PS} = 0.67$ for linear PS. This is related to a lower hydrodynamic volume ($V_h \sim [\eta]M$) occupied by star polymer due to their higher compaction compared with linear polymers of the same molar mass. Therefore, lower α value of star PS confirms the branched character of the polymers synthesized from TTC-4 CTA. For each slices of LogM, the quadratic equation that results from Eq 1 and Eq 2 was solved for values of ε equal to either 0.5, 1.0 or 1.5 in order to plot the value of number of arms *f* as a function of molar mass (Figure S9). Whatever the chosen ε value, *f* is above 2, which indicates that PS synthesized from TTC-4 are not analogous to linear PS. For the intermediate $\varepsilon = 1$ value, *f* ranges between 2.8 and 3.8 (Fig S9). Consequently, in the further part of the work, the macroCTA synthesized from TTC-4 CTA will be considered as star polymers and the ones synthesized from TTC-1 CTA as linear polymers (see Scheme 1 and Table 1).

Synthesis and characterization of P(S-*co*-BzMA)-*b*-POEGA block copolymers.

Block copolymers (BCP) consisting of a hard block of statistical copolymer of styrene and benzyl methacrylate, and a soft ion-conductive block of poly(oligo(ethylene glycol) methyl ether acrylate) (POEGA) were synthesized by chain extension of linear and star first blocks described in the previous

part (see Table 2).RAFT polymerization of OEGA was performed in bulk using P(S-*co*-BzMA) as macro-CTA and AIBN as initiator (Scheme 1). This protocol implies a good solubility of the macro-CTA in OEGA. This is the interest of PBzMA or P(S-*co*-BzMA) copolymers which are soluble in OEGA while solubilisation of PS in OEGA requires the addition of 1,4-dioxane solvent (see experimental part). ^{1}H NMR of both *s*-$A_{0.62}$ star precursor and associated *sc*-$(A_{0.62})_{0.80}B_{0.20}$ star comb-like block copolymer is displayed in Figure 4. The weight fraction of POEGA in BCP was derived from molar fraction of POEGA calculated from the ^{1}H NMR integrals (see Eq S20, Table 2). Interestingly, DOSY NMR of *sc*-$(A_{0.62})_{0.80}B_{0.20}$ block copolymer displays only one diffusion coefficient correlated with ^{1}H NMR signals of both P(S-*co*-BzMA) and POEGA moieties (Figure 4). This confirms the successful preparation of block copolymers, which was corroborated by the shift of SEC traces towards higher values of Log*M* between initial macroCTA and final BCP from both linear and star precursors (Figure S11-14). However, it should be noted that upon targeting intermediate OEGA conversion from star P(S-*co*-BzMA) macroCTA in bulk with high initial ratio of [OEGA]/[macroCTA] the final polymer was not soluble (gel-like) and could not be accurately analyzed by SEC (*sc*-$(A_{0.62})_{0.23}B_{0.77}$ sample in Table 2). This can be explained by star−star coupling by radical-radical combination reactions producing high molar mass hyper-branched structures, as previously reported for R-core mediated RAFT polymerization.[39]

Table 2. Features of the AB Linear Comb-like and Star Comb-like Diblock Copolymers Synthesized from the macro-CTA reported in Table 1

macroCTA	$\frac{[OEGA]_0}{[macroCTA]_0}$	**Conv. (%)**	W_{POEGA}[a]	$M_{n,theo}$[b] (kg·mol^{-1})	$M_{n,MALLS}$ (kg·mol^{-1})	$Đ_{MALLS}$	**BCP**[c]
***l*-A$_0$**	102	77[e]	0.68	59	41	1.20	***lc*-(A$_0$)$_{0.32}$B$_{0.68}$**
***l*-A$_{0.59}$**	41	94[e]	0.29	48	41	1.10	***lc*-(A$_{0.59}$)$_{0.71}$B$_{0.29}$**
***s*-A$_{0.62}$**	1525	54	0.77	530	*n.a.* [d]	*n.a.* [d]	***sc*-(A$_{0.62}$)$_{0.23}$B$_{0.77}$**
***s*-A$_{0.62}$**	175	98[e]	0.27	219	414	1.31	***sc*-(A$_{0.62}$)$_{0.73}$B$_{0.27}$**
***s*-A$_{0.62}$**	1525	13	0.20	153	155	1.22	***sc*-(A$_{0.62}$)$_{0.80}$B$_{0.20}$**
***s*-A$_{0.43}$**	1523	4	0.16	95	109	1.31	***sc*-(A$_{0.43}$)$_{0.84}$B$_{0.16}$**

[a] W_{POEGA} is the weight fraction of POEGA in the block copolymer after purification, as determined from the molar fraction calculated from ^{1}H NMR spectra (see Eq. S19).
[b] Theoretical molar mass determined from Eq. S14.
[c] *s*- and *l*- represents the star and linear polymers respectively.
[d] The SEC analysis was not applicable as the solubility of samples was too low and RI signal too weak to be reliable.
[e] Experiment performed in solution (1:1 v/v 1,4 dioxane:OEGA).

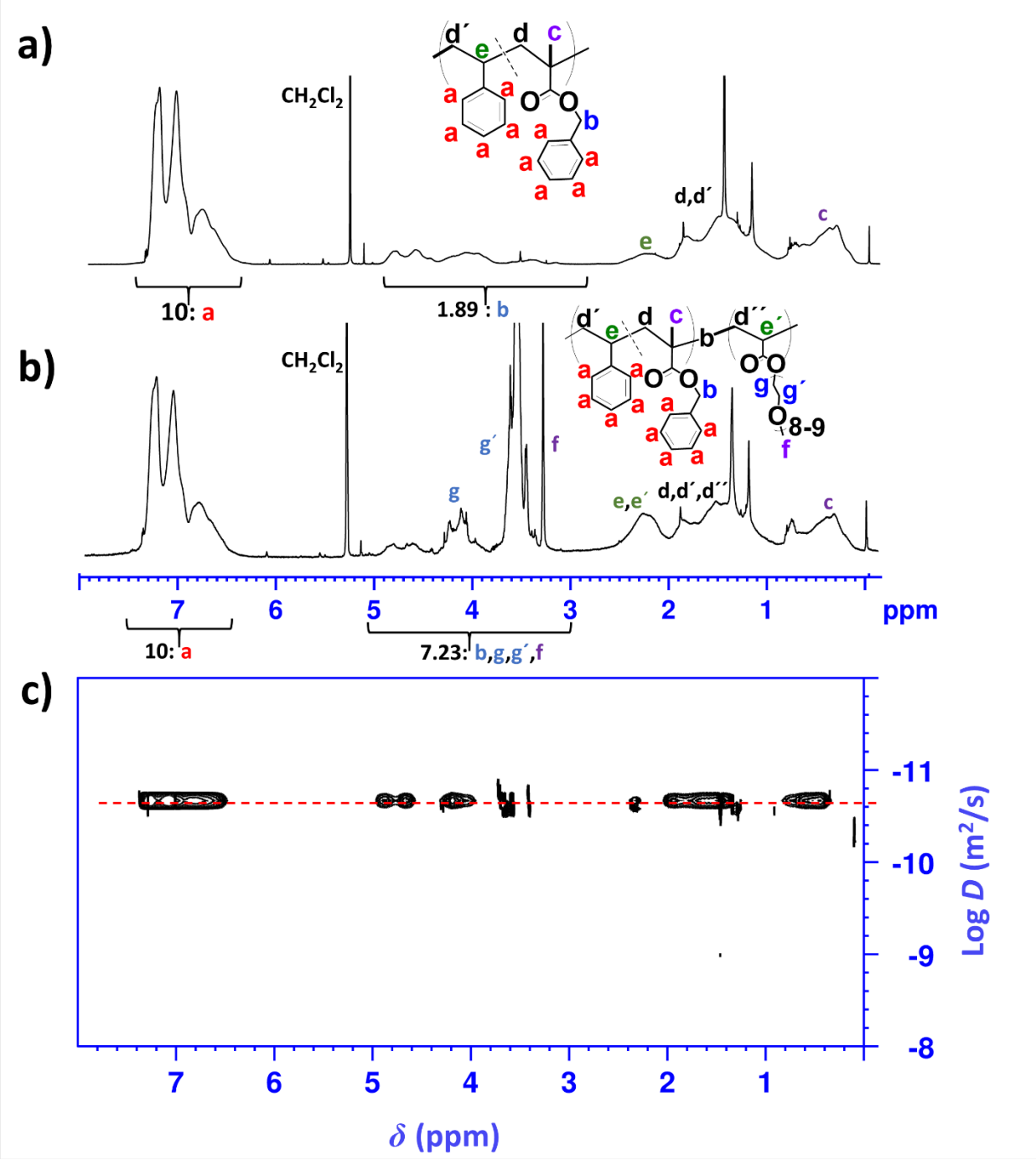

Figure 4.[1]H NMR spectra of a) *s*-$A_{0.62}$ and b) *sc*-$(A_{0.62})_{0.80}B_{0.20}$ in CD_2Cl_2 ([polymer] = 10 mg·mL^{-1}). Numbers correspond to the integrals of signals. c) DOSY NMR Spectrum: diffusion coefficient (D) versus chemical shift (δ) of *sc*-$(A_{0.62})_{0.80}B_{0.20}$.

Conductivity versus morphology.

The temperature-dependent ion conductivities which is a critical parameter for application in solid state batteries, was evaluated by EIS measurements. Conductivity versus temperature curves are

shown in Figure 5. As expected, in all samples, conductivity decreased with decreasing temperature due to a reduced segmental chain mobility at lower temperatures. Another observable trend was that conductivity increased with increasing volume fraction of the POEGA conducting phase, ϕ_c (see inset graph in Figure 5, Table S4). The conductivity of *sc*-$(A_{0.43})_{0.84}B_{0.16}$ copolymer was significantly lower, probably due to a weakly percolating POEGA conducting phase with such low ϕ_c.

The conductivity data versus temperature were fitted with either the Vogel-Fulcher-Tammann (VFT) or the Arrhenius models, thus pointing out different ion transport mechanisms. The VFT model depicts a coupling between the polymer chain segmental motion and the ion transport that scales with temperature. [40] The expression is

$$\sigma = \sigma_0 exp\left(-\frac{B}{R(T-T_0)}\right), \qquad 3$$

where B is the pseudo activation energy for ion transport, σ_0 is a prefactor related to the number of charge carriers present in the electrolyte, R is the gas constant, and T_0 is the Vogel temperature. T_0 is a reference temperature at which the configurational entropy of the polymer matrix becomes zero and is empirically related to the polymer T_g. On the other hand, the Arrhenius model is associated to a Grotthuss mechanism of ion transport.[41] The corresponding expression is

$$\sigma = \sigma_0 exp\left(-\frac{E_a}{RT}\right), \qquad 4$$

with E_a the activation energy, which differs from the VFT pseudo activation energy. The model selection was based on the shape of the conductivity curves on Arrhenius plot, as described hereafter. Data collected on the BCPEs with the larger POEGA blocks (cf. Table 2), i.e. *sc*-$(A_{0.62})_{0.23}B_{0.77}$, *sc*-$(A_{0.62})_{0.73}B_{0.27}$, *sc*-$(A_{0.62})_{0.80}B_{0.20}$, and *lc*-$(A_0)_{0.32}B_{0.68}$, were fitted with the VFT model to account for the curvature on the Arrhenius plot. Thus indicating a significant role of the POEGA segmental motion on the ion transport. The values of T_0 (in °C) are presented in Table S3 together with the corresponding conductive block T_g measured by DSC. The T_0 range between 40 and 60 °C below the T_g which agrees with empirical value of 50 °C reported in the literature.[40] The two BCPEs with shorter POEGA blocks (cf. Table 2), i.e. *sc*-$(A_{0.43})_{0.84}B_{0.16}$ and *lc*-$(A_{0.59})_{0.71}B_{0.29}$ do not exhibit evident curvature, then Arrhenius model was used to fit the data. Considering those two samples, linear and star comb-like based, one can expect that POEGA segmental motion is limited due the reduced block molar masses which remains anchored to the high T_g domains. Since the morphology of the self-assembled BCPEs is known to play a role on ion conductivity, the bulk morphologies of the BCPE films were investigated using SAXS and TEM.

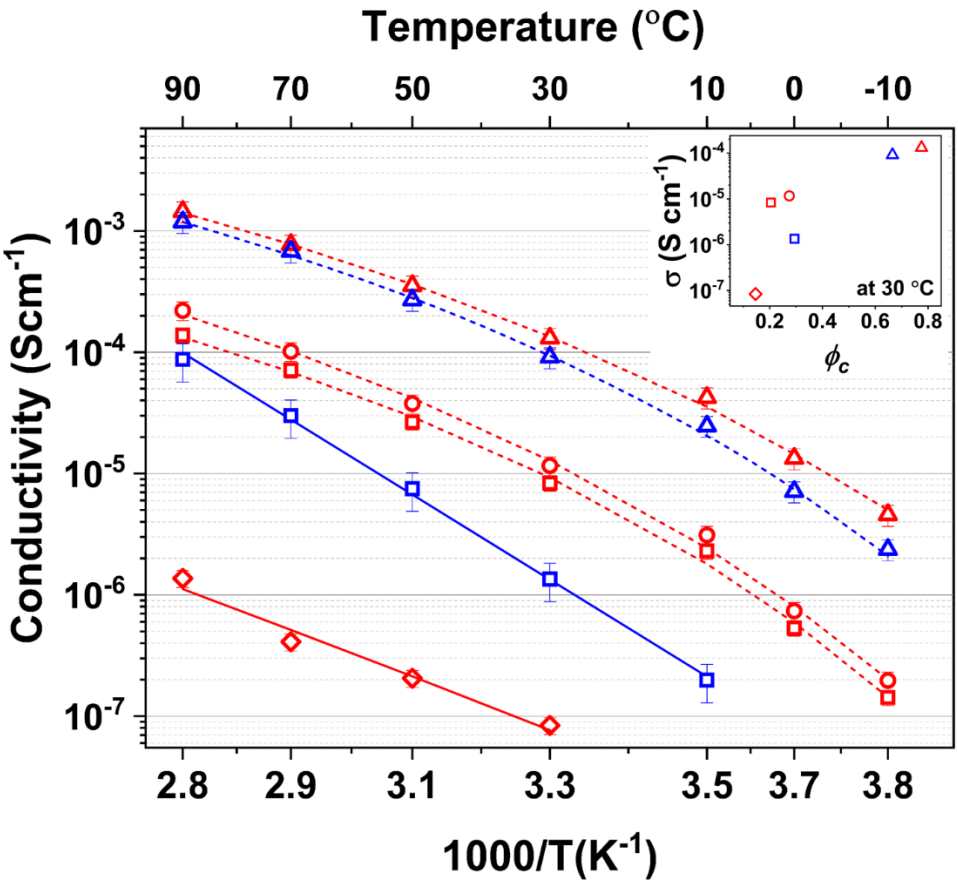

Figure 5. Temperature-dependent ionic conductivity derived from the EIS measurements of BCPEs: (Δ) *sc*-$(A_{0.62})_{0.23}B_{0.77}$, (○) *sc*-$(A_{0.62})_{0.73}B_{0.27}$, (□) *sc*-$(A_{0.62})_{0.80}B_{0.20}$, (◊) *sc*-$(A_{0.43})_{0.84}B_{0.16}$, (Δ) *lc*-$(A_0)_{0.32}B_{0.68}$, (□) *lc*-$(A_{0.59})_{0.71}B_{0.29}$. Solid lines represent Arrhenius fits and the dashed lines represent VFT fits. Inset graph shows plot of σ versus ϕ_c of conducting phase for star comb-like (red) and linear comb-like (blue) BCPEs.

SAXS profiles were collected for linear and star comb-like BCPs for temperatures ranging from 25 to 100 °C. Linear BCPs show no structural peak (exemplified with sample *lc*-$(A_{0.59})_{0.71}B_{0.29}$ in Figure S17a) while star BCPEs show a broad single peak (exemplified with sample *sc*-$(A_{0.62})_{0.80}B_{0.20}$ in Figure S18a) thus indicating poor phase separation of the BCPs. After blending the BCP with LiTFSI salt (at ratio [EO]/[Li] =15), low intensity structural peaks were observed at 25 °C indicating phase separation of the individual blocks. Upon annealing at 100 °C, slightly shifted higher intensity structural peaks could be observed indicating stronger phase separation. Several reports have indicated that addition of lithium salt increases the effective Flory−Huggins interaction parameter (χ_{eff}) between the polymer blocks as well as the stiffness of the chains comprising the ion-conducting domain.[42-44] In order to follow any possible phase transition that may be associated with temperature-dependent changes, *in-situ* SAXS measurements were performed while cooling stepwise to 30 °C (see Figure S17b and Figure S18b). However, there was no drastic re-definition of the structural patterns thus signifying that the samples retain their morphologies after annealing.

The following structural characterization was performed on BCPEs, after a temperature annealing at 100 °C, by SAXS (Figure 6) and bright field TEM (Figure 7). For star comb-like series, the scattering profiles of *sc*-$(A_{0.62})_{0.73}B_{0.27}$ and *sc*-$(A_{0.62})_{0.80}B_{0.20}$ BCPEs (Figure 6a) show primary peaks at $q^* \approx 0.15$ nm^{-1} and $q^* \approx 0.16$ nm^{-1} respectively with higher order peaks positioned at $2q^*$, $3q^*$, $4q^*$ and $5q^*$ which are signatures of lamellar microstructure (LAM). The characteristic LAM periods were calculated from $d = 2\pi / q^*$ and given as $d = 41$ nm and 39 nm respectively. In case of *sc*-$(A_{0.43})_{0.84}B_{0.16}$, low intensity and broad structural peaks *at* q^*, $2q^*$, $3q^*$ indicates also a LAM pattern, with d = 58 nm. TEM pictures collected on those three samples confirm the SAXS findings, displaying evident LAM morphologies (Figure 7 b, c and d). Nevertheless, TEM images bring additional information on the quality of the ordering. Indeed, samples *sc*-$(A_{0.62})_{0.73}B_{0.27}$ and *sc*-$(A_{0.62})_{0.80}B_{0.20}$ feature long-range LAM ordering. On the other hand, *sc*-$(A_{0.43})_{0.84}B_{0.16}$ BCPE ordering is limited and punctuated with inverted hexagonal cylinders (HEX') phases (see arrow markers in Figure 7d). This later feature might act as dead ends thus impeding ion transport. The scattering curve collected on sample *sc*-$(A_{0.62})_{0.23}B_{0.77}$ (Figure 6a) shows a broad primary peak, $q^* \approx 0.14$ nm^{-1} and secondary peak at $\sqrt{7}\, q^*$. The secondary peak indicates that the morphology is not LAM and the TEM image (Figure 7a) shows evident spherical objects dispersed in the POEGA conducting phase. A characteristic sphere-to-sphere distance, d = 45 nm is estimated from $d = 2\pi/ q^*$.

For linear comb-like BCPE series, TEM image collected on sample *lc*-$(A_0)_{0.32}B_{0.68}$ (Figure 7e) shows an evident HEX morphology with a majority POEGA conducting phase. This is confirmed by SAXS (Figure 6b) with structural peaks positioned at $q^* \approx 0.17$ nm^{-1}, $2q^*$, $\sqrt{7}q^*$ and $\sqrt{13}q^*$. A cylinder-to-cylinder distance d = 43 nm is calculated with $d = 4\pi/\sqrt{3}q^*$. The SAXS profile measured on sample *lc*-$(A_{0.59})_{0.71}B_{0.29}$ (Figure 6b) displays peaks at $q^* \approx 0.18$ nm^{-1}, $2q^*$, $3q^*$, and $4q^*$ indicative of a LAM morphology with d = 35 nm. This is also in agreement with the TEM image (Figure 7f) exhibiting swirly short-range ordered lamella.

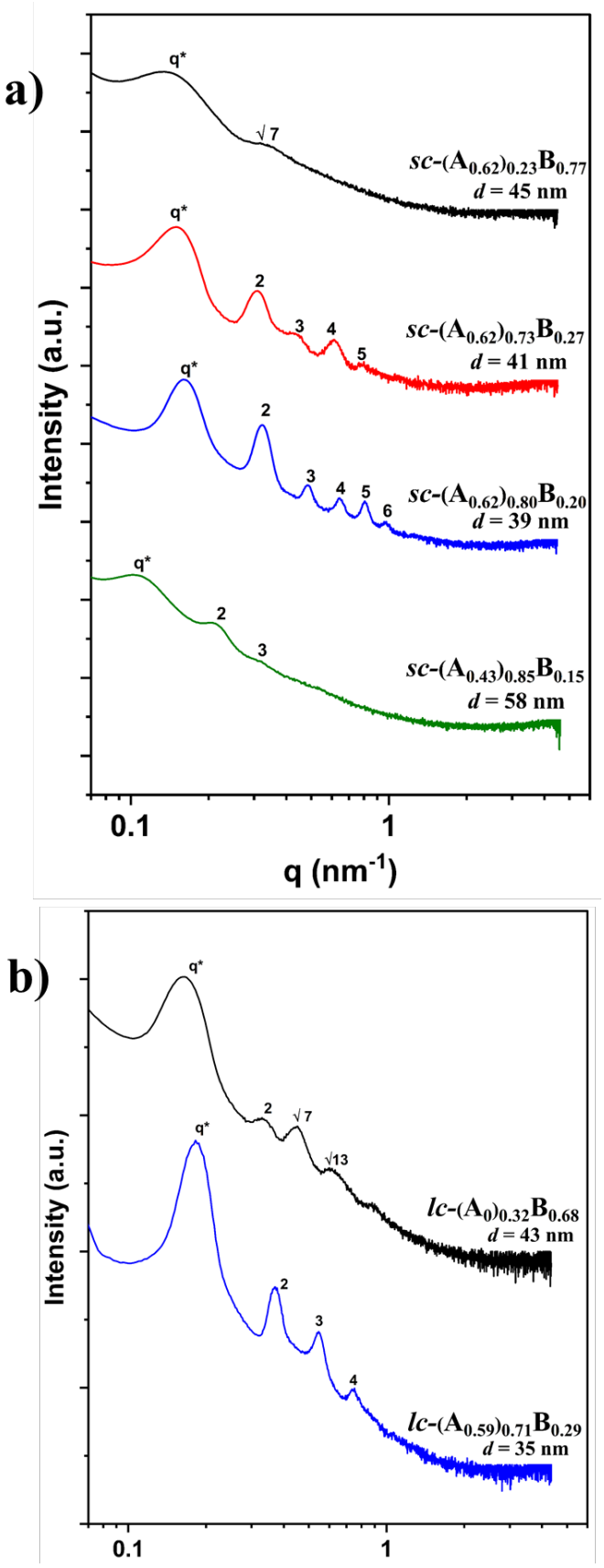

Figure 6. SAXS profiles of BCPEs at 30 °C after cooling. a) star comb-like BCPE b) linear comb-like BCPE.

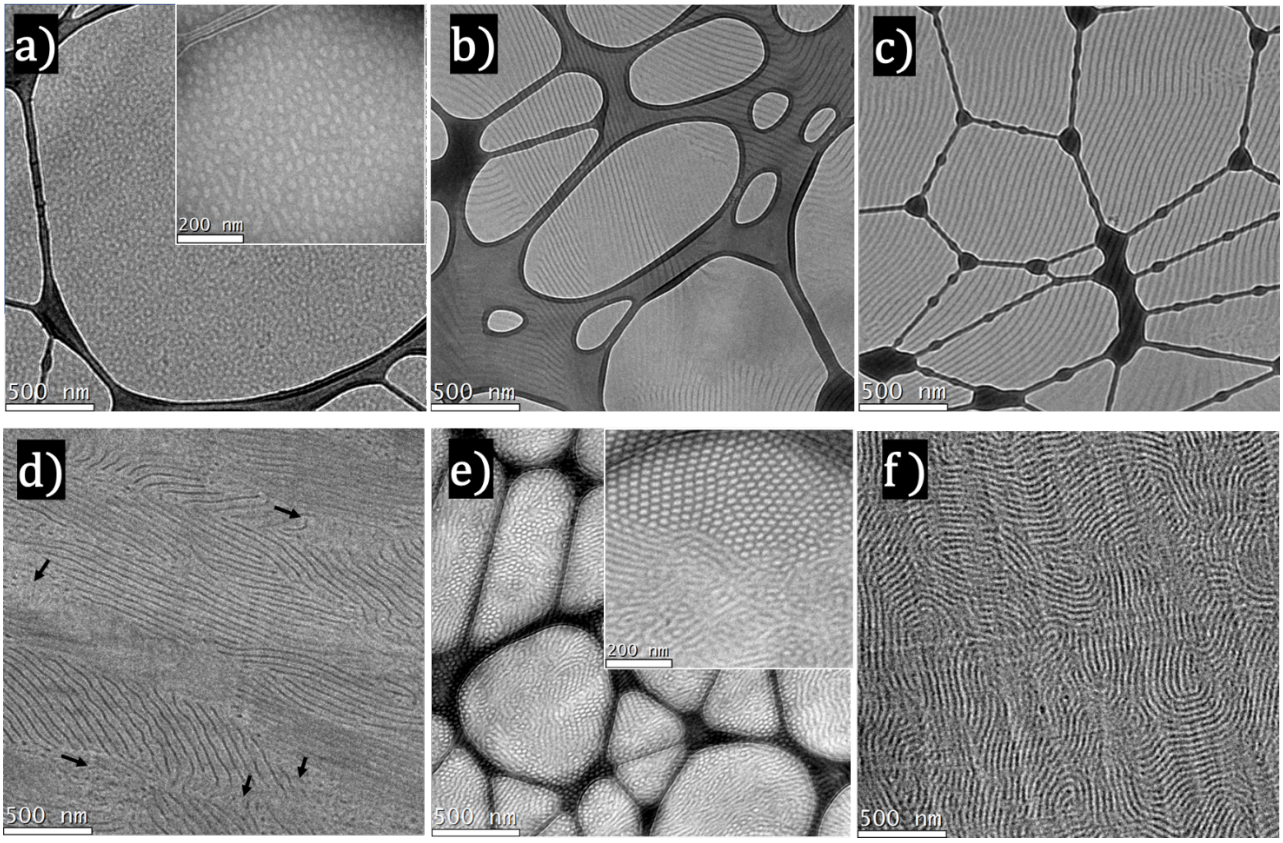

Figure 7. TEM images for annealed star comb-like BCPE (Top) and linear comb-like BCPEs (bottom) prepared by mixing LiTFSI and BCP with varying ratio of final conducting volume fraction of POEGA/LiTFSi conducting phase (ϕ_c). a) *sc*-$(A_{0.62})_{0.23}B_{0.77}$, $\phi_c = 0.78$ (Sphere), b) *sc*-$(A_{0.62})_{0.73}B_{0.27}$, $\phi_c = 0.27$ (LAM), c) *sc*-$(A_{0.62})_{0.80}B_{0.20}$, $\phi_c = 0.20$ (LAM), d) *sc*-$(A_{0.43})_{0.84}B_{0.16}$, $\phi_c = 0.15$ (LAM and HEX'), e) *lc*-$(A_0)_{0.32}B_{0.68}$, and f) *lc*-$(A_{0.59})_{0.71}B_{0.29}$, $\phi_c = 0.68$ (HEX) and $\phi_c = 0.29$ (LAM) respectively. Black arrows show regions of hexagonal cylinders (HEX') with POEGA minority phase.

Despite a rather similar composition the star BCPEs *sc*-$(A_{0.62})_{0.73}B_{0.27}$ and *sc*-$(A_{0.62})_{0.80}B_{0.20}$ and the linear *lc*-$(A_{0.59})_{0.71}B_{0.29}$ display a stark difference. The star BCPEs exhibit straight and long-range LAM morphologies (Figure 7b and Figure 7c, additional micrographs have been provided in supporting information Figures S19-S21), resulting from dense self-assembly of multiple arms of the star BCPE. Similar results have been reported for miktoarm star PS-*b*-$(PEO)_3$ BC by Lee *et al.*[25] Consequently, this reduced tortuosity leads to a higher ionic conductivity compared to the linear *lc*-$(A_{0.59})_{0.71}B_{0.29}$ BCPE. To further depict the influence of morphologies on ionic conductivity, we assumed that (i) the overall mobility of ions in the electrolytes is facilitated by the segmental motion of the EO side chains and hence conductivity can be correlated to ϕ_c as discussed previously; (ii) the

POEGA phase in the BCPEs considered separately presents all the same ionic conductivity, σ_0, at a specific salt concentration. Based on these assumptions, σ, the BCPE conductivity, can be define as[14]

$$\sigma = \frac{f}{\tau}\phi_c\sigma_0 \ , \qquad 5$$

where τ is a local tortuosity factor, *i.e.* the ratio of the effective pathway required for ion transport through the electrolyte thickness, and f is a morphological factor to quantify the global grain alignment in the direction of the electric field. Values of $f\tau^{-1}$ for LAM, HEX and sphere (BCC) morphologies have been reported in literature based on effective medium theory (see Table S6). [45]

First, POEGA conductivity values, σ_0, was evaluated at 30 °C with Eq 5 by using the experimental conductivities, σ, of *sc*-$(A_{0.62})_{0.23}B_{0.77}$ and *lc*-$(A_0)_{0.32}B_{0.68}$ and the theoretical values of $f\tau^{-1}$ of BCC sphere and HEX morphologies as reported in Table S4. *sc*-$(A_{0.62})_{0.23}B_{0.77}$ and *lc*-$(A_0)_{0.32}B_{0.68}$ samples were chosen as references because the observed morphologies feature continuous POEGA conducting majority phases. Also, Balsara and coworkers have shown that the conductivity models fit better the experimental values at higher ϕ_c.[14] σ_0 values of 1.87×10^{-4} and 2.05×10^{-4} S.cm^{-1} were obtained respectively from *sc*-$(A_{0.62})_{0.23}B_{0.77}$ (spheres) and *lc*-$(A_0)_{0.32}B_{0.68}$ (HEX). Both values are relatively close thus reinforcing the previous assumptions. Also, as expected, this indicates that star and linear architectures do not impact significantly the ion conductivity of the majority POEGA phase, when POEGA is the BCP outer blocks. Here after, the σ_0 averaged value of 1.96×10^{-4} S.cm^{-1} at 30 °C will be used.

In order to evaluate the influence of the nanometer morphology, the conductivity of each BCPEs, σ, were normalized by $\phi_c\sigma_0$, which theoretically equals to $f\tau^{-1}$, representative of a given model morphology (cf. Eq 5 and Table S5). All the experimental values of $f\tau^{-1}$ are displayed in Figure 8, in addition, for comparison, the theoretical value of $f\tau^{-1} = 2/3$, for LAM, is plotted as short dashed line (black) across the ϕ_c region where LAM phases were observed. In Figure 8, experimental $f\tau^{-1}$ of *sc*-$(A_{0.62})_{0.73}B_{0.27}$, *sc*-$(A_{0.62})_{0.80}B_{0.20}$ and *lc*-$(A_{0.59})_{0.71}B_{0.29}$ are significantly lower than the theoretical 2/3. An explanation for those deviations is that defects, such as grain boundaries and lamellar fluctuations, constitute extra tortuosity, thus $\tau > 1$.[25, 46] Finally, the tortuosity factors can be evaluated from Eq 5, considering $f = 2/3$. Values of $\tau = 3.2$, 3.1 and 28.2 are obtained respectively for star (*sc*-$(A_{0.62})_{0.73}B_{0.27}$, *sc*-$(A_{0.62})_{0.80}B_{0.20}$) and linear (*lc*-$(A_{0.59})_{0.71}B_{0.29}$) BCPEs. The significantly larger values found for the linear BCPE can be explained by the swirly lamellar observed by TEM (see Figure 7f). Indeed, star BCPEs encompasses unique macromolecular self-organization that affect the structural range and connectivity of ordered grains so that the ionic pathway is less tortuous than the linear ones.

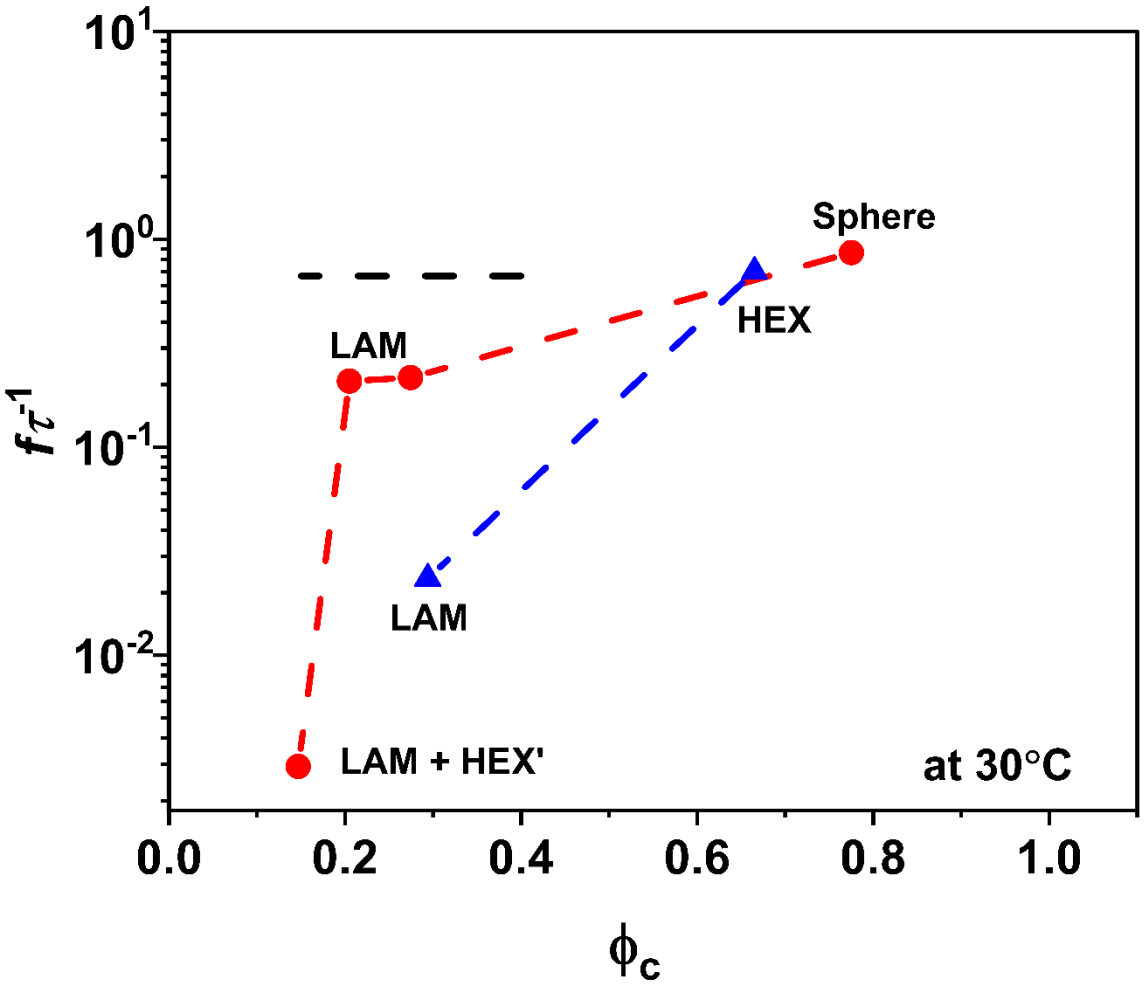

Figure 8. Normalized Conductivity ($\sigma/(\phi_c\sigma_0) = f\tau^{-1}$) at 30°C as a function of ϕ_c for star (●) and linear (▲) BCPEs. The solid black line (- - -) corresponds to theoretical values $f\tau^{-1}$ for lamellar in Table S6.

Conclusion

Two series of P(S-*co*-BzMA)-*b*-POEGA block copolymers of star and linear comb-like architecture were successfully synthesized by RAFT polymerization. The addition of a small amount of styrene (minimum 6 mol%) was needed to control BzMA polymerization mediated by the tetrafunctional chain transfer agent. S and BzMA comonomers were homogeneously distributed along the polymer chain for a wide range of monomer feed ratios ($f_{BzMA,0}$ from 0 to 0.94) to produce statistical star copolymers with tunable properties. Mark-Houwink-Sakurada plot and determination of the *g* contraction factor confirmed the star-like architecture of the PS macroCTA. The block's phase segregation was induced by addition of lithium salt and lamellar, hexagonal cylinder and sphere phases have been observed by TEM and SAXS. As expected, the conductivity increased with the volume fraction of POEGA/LiTFSI conducting phase, however a strong dependence on the self-assembled morphologies is observed. Focussing on the quality of the lamellar morphology produced

by star and linear BCPEs a correlation can be done between the generated tortuosity and ionic conductivity. Indeed, the star comb-like BCPs with ~30 wt-% of POEGA/LiTFSI conductive phase gave rise to highly ordered lamellar structures compared to the swirly lamellae of linear analogue. Consequently, the reduced lamellae tortuosity of self-assembled star comb-like BCPs improved the lithium conductivity by more than 8 times at 30°C.

Supporting Information

Monomer conversion, formulas and experimental data for calculation of reactivity ratios, Mark-Houwink-Sakurada plot for star polymer, SEC chromatograms, kinetics for chain extension with OEGA monomer, DSC curves, formulas for calculation of blocks and conductive phase volume fractions, pictures of self-standing transparent films, SAXS of in-situ annealing of BCPE films, additional TEM pictures, morphology factor, f, and tortuosity, τ are supplied as Supporting Information.

Acknowledgement

This project was carried out within the POLYSTORAGE European training network and have received funding from the European Union's Horizon 2020 research and innovation programme under the Marie Skłodowska-Curie grant agreement No 860403. We acknowledge the provision of facilities and technical support by Aalto University at OtaNano-Nanomicroscopy Center (Aalto-NMC). Abdel Khoukh is also gratefully acknowledged for performing the DOSY NMR experiments.

Conflicts of interest

The authors declare no conflict of interest.

References.

(1) Nair, J. R.; Imholt, L.; Brunklaus, G.; Winter, M. Lithium Metal Polymer Electrolyte Batteries: Opportunities and Challenges. *The Electrochemical Society Interface* **2019,** *28* (2), 55-61, DOI: https://iopscience.iop.org/article/10.1149/2.F05192if.
(2) Hallinan, D. T.; Balsara, N. P. Polymer Electrolytes. *Annual Review of Materials Research* **2013,** *43*, 503-525, DOI: https://doi.org/10.1146/annurev-matsci-071312-121705.
(3) Hallinan, D. T.; Mullin, S. A.; Stone, G. M.; Balsara, N. P. Lithium Metal Stability in Batteries with Block Copolymer Electrolytes. *Journal of The Electrochemical Society* **2013,** *160* (3), A464-A470, DOI: https://iopscience.iop.org/article/10.1149/2.030303jes.
(4) Hashim, N. H. A. M.; Subban, R. H. Y. Studies on Conductivity, Structural and Thermal Properties of PEO-LiTFSI Polymer Electrolytes Doped with EMImTFSI Ionic Liquid. *AIP Conference Proceedings* **2018,** *2031* (1), 0200211 - 0200216, DOI: https://doi.org/10.1063/1.5066977.

(5) Phan, T. N. T.; Issa, S.; Gigmes, D. Poly(ethylene oxide)-Based Block Copolymer Electrolytes for Lithium Metal Batteries. *Polymer International* **2019,** *68* (1), 7-13, DOI: https://doi.org/10.1002/pi.5677.
(6) Choi, Y. K.; Bae, Y. H.; Kim, S. W. Star-Shaped Poly(ether−ester) Block Copolymers: Synthesis, Characterization, and Their Physical Properties. *Macromolecules* **1998,** *31* (25), 8766-8774, DOI: https://pubs.acs.org/doi/abs/10.1021/ma981069i.
(7) Croce, F.; Appetecchi, G. B.; Persi, L.; Scrosati, B. Nanocomposite Polymer Electrolytes for Lithium Batteries. *Nature* **1998,** *394* (6692), 456-458, DOI: https://doi.org/10.1038/28818.
(8) Bergman, M.; Bergfelt, A.; Sun, B.; Bowden, T.; Brandell, D.; Johansson, P. Graft Copolymer Electrolytes for High Temperature Li-battery Applications, Using Poly(methyl methacrylate) Grafted Poly(ethylene glycol)methyl Ether Methacrylate and Lithium bis(trifluoromethanesulfonimide). *Electrochimica Acta* **2015,** *175*, 96-103, DOI: https://doi.org/10.1016/j.electacta.2015.01.226.
(9) Tikhonov, P. A.; Vasilenko, N. G.; Muzafarov, A. A. M. Multiarm Star Polymers. Fundamental Aspects. A Review. *Doklady Chemistry* **2021,** *496* (1), 1-17, DOI: https://doi.org/10.1134/S001250082101002X.
(10) Young, W.-S.; Kuan, W.-F.; Epps, I. I. I. T. H. Block copolymer electrolytes for rechargeable lithium batteries. *Journal of Polymer Science Part B: Polymer Physics* **2014,** *52* (1), 1-16, DOI: https://doi.org/10.1002/polb.23404.
(11) Xue, Z.; He, D.; Xie, X. Poly(ethylene oxide)-Based Electrolytes for Lithium-ion Batteries. *Journal of Materials Chemistry A* **2015,** *3* (38), 19218-19253, DOI: https://doi.org/10.1039/C5TA03471J.
(12) Simone, P. M.; Lodge, T. P. Phase Behavior and Ionic Conductivity of Concentrated Solutions of Polystyrene-Poly(ethylene oxide) Diblock Copolymers in an Ionic Liquid. *ACS Applied Materials & Interfaces* **2009,** *1* (12), 2812-2820, DOI: https://doi.org/10.1021/am900555f.
(13) Chintapalli, M.; Chen, X. C.; Thelen, J. L.; Teran, A. A.; Wang, X.; Garetz, B. A.; Balsara, N. P. Effect of Grain Size on the Ionic Conductivity of a Block Copolymer Electrolyte. *Macromolecules* **2014,** *47* (15), 5424-5431, DOI: https://doi.org/10.1021/ma501202c.
(14) Galluzzo, M. D.; Loo, W. S.; Wang, A. A.; Walton, A.; Maslyn, J. A.; Balsara, N. P. Measurement of Three Transport Coefficients and the Thermodynamic Factor in Block Copolymer Electrolytes with Different Morphologies. *The Journal of Physical Chemistry B* **2020,** *124* (5), 921-935, DOI: https://doi.org/10.1021/acs.jpcb.9b11066.
(15) Loo, W. S.; Galluzzo, M. D.; Li, X.; Maslyn, J. A.; Oh, H. J.; Mongcopa, K. I.; Zhu, C.; Wang, A. A.; Wang, X.; Garetz, B. A.; Balsara, N. P. Phase Behavior of Mixtures of Block Copolymers and a Lithium Salt. *The Journal of Physical Chemistry B* **2018,** *122* (33), 8065-8074, DOI: https://doi.org/10.1021/acs.jpcb.8b04189.
(16) Chakraborty, S.; Jiang, X.; Hoffman, Z. J.; Sethi, G. K.; Zhu, C.; Balsara, N. P.; Villaluenga, I. Reversible Changes in the Grain Structure and Conductivity in a Block Copolymer Electrolyte. *Macromolecules* **2020,** *53* (13), 5455-5464, DOI: https://doi.org/10.1021/acs.macromol.0c00466.
(17) Chintapalli, M.; Higa, K.; Chen, X. C.; Srinivasan, V.; Balsara, N. P. Simulation of Local Ion transport in Lamellar Block Copolymer Electrolytes Based on Electron Micrographs. *Journal of Polymer Science Part B: Polymer Physics* **2017,** *55* (3), 266-274, DOI: https://doi.org/10.1002/polb.24268.
(18) Chintapalli, M.; Le, T. N. P.; Venkatesan, N. R.; Mackay, N. G.; Rojas, A. A.; Thelen, J. L.; Chen, X. C.; Devaux, D.; Balsara, N. P. Structure and Ionic Conductivity of Polystyrene-block-poly(ethylene oxide) Electrolytes in the High Salt Concentration Limit. *Macromolecules* **2016,** *49* (5), 1770-1780, DOI: https://doi.org/10.1021/acs.macromol.5b02620.
(19) Devaux, D.; Glé, D.; Phan, T. N. T.; Gigmes, D.; Giroud, E.; Deschamps, M.; Denoyel, R.; Bouchet, R. Optimization of Block Copolymer Electrolytes for Lithium Metal Batteries. *Chemistry of Materials* **2015,** *27* (13), 4682-4692, DOI: https://doi.org/10.1021/acs.chemmater.5b01273.

(20) Butzelaar, A. J.; Liu, K. L.; Röring, P.; Brunklaus, G.; Winter, M.; Theato, P. A Systematic Study of Vinyl Ether-Based Poly(Ethylene Oxide) Side-Chain Polymer Electrolytes. *ACS Applied Polymer Materials* **2021,** *3* (3), 1573-1582, DOI: https://doi.org/10.1021/acsapm.0c01398.
(21) Ruzette, A.-V. r. G.; Soo, P. P.; Sadoway, D. R.; Mayes, A. M. Melt-Formable Block Copolymer Electrolytes for Lithium Rechargeable Batteries. *Journal of The Electrochemical Society* **2001,** *148* (6), 537 - 543, DOI: https://iopscience.iop.org/article/10.1149/1.1368097.
(22) Bergfelt, A.; Rubatat, L.; Brandell, D.; Bowden, T. Poly(benzyl methacrylate)-poly (oligo ethylene glycol) Methyl Ether Methacrylate Triblock-copolymers as Solid Electrolyte for Lithium Batteries. *Solid State Ion.* **2018,** *321*, 55-61, DOI: https://doi.org/10.1016/j.ssi.2018.04.006.
(23) Park, J.; Jang, S.; Kon Kim, J. Morphology and Microphase Separation of Star Copolymers. *Journal of Polymer Science Part B: Polymer Physics* **2015,** *53* (1), 1-21, DOI: https://doi.org/10.1002/polb.23604.
(24) Liffland, S.; Hillmyer, M. A. Enhanced Mechanical Properties of Aliphatic Polyester Thermoplastic Elastomers through Star Block Architectures. *Macromolecules* **2021,** *54* (20), 9327-9340, DOI: https://doi.org/10.1021/acs.macromol.1c01357.
(25) Lee, D.; Jung, H. Y.; Park, M. J. Solid-State Polymer Electrolytes Based on AB3-Type Miktoarm Star Copolymers. *ACS Macro Letters* **2018,** *7* (8), 1046-1050, DOI: https://doi.org/10.1021/acsmacrolett.8b00474.
(26) Wang, S.; Wang, A.; Yang, C.; Gao, R.; Liu, X.; Chen, J.; Wang, Z.; Zeng, Q.; Liu, X.; Zhou, H.; Zhang, L. Six-arm Star Polymer Based on Discotic Liquid Crystal as High Performance All-solid-state Polymer Electrolyte for Lithium-ion Batteries. *J. Power Sources* **2018,** *395*, 137-147, DOI: https://doi.org/10.1016/j.jpowsour.2018.05.069.
(27) Niitani, T.; Amaike, M.; Nakano, H.; Dokko, K.; Kanamura, K. Star-Shaped Polymer Electrolyte with Microphase Separation Structure for All-Solid-State Lithium Batteries. *Journal of The Electrochemical Society* **2009,** *156*, 577 - 583, DOI: https://iopscience.iop.org/article/10.1149/1.3129245.
(28) Tong, Y.; Chen, L.; He, X.; Chen, Y. Sequential Effect and Enhanced Conductivity of Star-shaped Diblock Liquid-crystalline Copolymers for Solid Electrolytes. *J. Power Sources* **2014,** *247*, 786-793, DOI: https://doi.org/10.1016/j.jpowsour.2013.08.139.
(29) Xie, H.-q.; Xie, D.; Liu, J. Solid Polymer Electrolyte Complexes of Polyoxyethylene-Containing Star-Shaped Block Copolymers and Copolymers with Uniform Grafts. *Polymer-plastics Technology and Engineering* **1989,** *28*, 355-369, DOI: https://doi.org/10.1080/03602558908048604.
(30) Bouchet, R.; Phan, T. N. T.; Beaudoin, E.; Devaux, D.; Davidson, P.; Bertin, D.; Denoyel, R. Charge Transport in Nanostructured PS–PEO–PS Triblock Copolymer Electrolytes. *Macromolecules* **2014,** *47* (8), 2659-2665, DOI: https://doi.org/10.1021/ma500420w.
(31) Rojas, A. A.; Inceoglu, S.; Mackay, N. G.; Thelen, J. L.; Devaux, D.; Stone, G. M.; Balsara, N. P. Effect of Lithium-Ion Concentration on Morphology and Ion Transport in Single-Ion-Conducting Block Copolymer Electrolytes. *Macromolecules* **2015,** *48* (18), 6589-6595, DOI: https://doi.org/10.1021/acs.macromol.5b01193.
(32) Mueller, A. H. E.; Yan, D.; Litvinenko, G.; Zhuang, R.; Dong, H. Kinetic Analysis of "Living" Polymerization Processes Exhibiting Slow Equilibria. 2. Molecular Weight Distribution for Degenerative Transfer (Direct Activity Exchange between Active and "Dormant" Species) at Constant Monomer Concentration. *Macromolecules* **1995,** *28* (22), 7335-7338, DOI: https://doi.org/10.1021/ma950887x.
(33) Charleux, B.; Nicolas, J.; Guerret, O. Theoretical Expression of the Average Activation−Deactivation Equilibrium Constant in Controlled/Living Free-Radical Copolymerization Operating via Reversible Termination. Application to a Strongly Improved Control in Nitroxide-Mediated Polymerization of Methyl Methacrylate. *Macromolecules* **2005,** *38* (13), 5485-5492, DOI: https://doi.org/10.1021/ma050087e.

(34) Beuermann, S.; Harrisson, S.; Hutchinson, R. A.; Junkers, T.; Russell, G. T. Update and Critical Reanalysis of IUPAC Benchmark Propagation Rate Coefficient Data. *Polymer Chemistry* **2022,** *13* (13), 1891-1900, DOI: https://doi.org/10.1039/D2PY00147K.
(35) Segall, I.; Dimonie, V. L.; El-Aasser, M. S.; Soskey, P. R.; Mylonakis, S. G. Core-shell Structured Latex Particles. I. Copolymerization of Styrene/benzyl Methacrylate as a Choice for Shell Material and Characterization of Poly(Ž butyl acrylate) Core Latex Particles. *Journal of Applied Polymer Science* **1995,** *58*, 385-399, DOI: https://doi.org/10.1002/app.1995.070580218.
(36) Zhang, C.; Lessard, B.; Maric, M. Synthesis and Characterization of Benzyl Methacrylate/Styrene Random Copolymers Prepared by NMP. *Macromolecular Reaction Engineering* **2010,** *4* (6-7), 415-423, DOI: https://doi.org/10.1002/mren.200900069.
(37) Striegel, A.; Yau, W. W.; Kirkland, J. J.; Bly, D. D. Polymer Architecture and Dilute Solution Thermodynamics. *Modern Size-Exclusion Liquid Chromatography* **2009**, 292-321, DOI: https://doi.org/10.1002/9780470442876.ch11.
(38) Bawn, C. E. H.; Grimley, T. B.; Wajid, M. A. High Polymer Solutions. Part IV.—The Intrinsic Viscosity-Molecular Weight Relationships in Mixed Solvents. *Transactions of the Faraday Society* **1950,** *46* (0), 1112-1120, DOI: https://doi.org/10.1039/TF9504601112.
(39) Stenzel-Rosenbaum, M.; Davis, T. P.; Chen, V.; Fane, A. G. Star-polymer Synthesis via Radical Reversible Addition–fragmentation Chain-transfer Polymerization. *Journal of Polymer Science Part A: Polymer Chemistry* **2001,** *39* (16), 2777-2783, DOI: https://doi.org/10.1002/pola.1256.
(40) Diederichsen, K. M.; Buss, H. G.; McCloskey, B. D. The Compensation Effect in the Vogel–Tammann–Fulcher (VTF) Equation for Polymer-Based Electrolytes. *Macromolecules* **2017,** *50* (10), 3831-3840, DOI: https://doi.org/10.1021/acs.macromol.7b00423.
(41) Kotobuki, M. Polymer Electrolytes. *Polymer Electrolytes: Characterization Techniques and Energy Applications* **2020**, 1-22, DOI: https://doi.org/10.1002/9783527805457.ch1.
(42) Gartner, T. E.; Morris, M. A.; Shelton, C. K.; Dura, J. A.; Epps, T. H. Quantifying Lithium Salt and Polymer Density Distributions in Nanostructured Ion-Conducting Block Polymers. *Macromolecules* **2018,** *51* (5), 1917-1926, DOI: https://doi.org/10.1021/acs.macromol.7b02600.
(43) Wang, J.-Y.; Chen, W.; Russell, T. P. Ion-Complexation-Induced Changes in the Interaction Parameter and the Chain Conformation of PS-b-PMMA Copolymers. *Macromolecules* **2008,** *41* (13), 4904-4907, DOI: https://doi.org/10.1021/ma800718z.
(44) Nakamura, I.; Wang, Z.-G. Salt-doped Block Copolymers: Ion Distribution, Domain Spacing and Effective χ Parameter. *Soft Matter* **2012,** *8* (36), 9356-9367, DOI: https://doi.org/10.1039/C2SM25606A.
(45) Hallinan, D. T.; Villaluenga, I.; Balsara, N. P. Polymer and Composite Electrolytes. *MRS Bulletin* **2018,** *43* (10), 759-767, DOI: https://doi.org/10.1557/mrs.2018.212.
(46) Kambe, Y.; Arges, C. G.; Patel, S.; Stoykovish, M. P.; Nealey, P. F. Ion Conduction in Microphase-Separated Block Copolymer Electrolytes. *The Electrochemical Society Interface* **2017,** *26* (1), 61-67, DOI: https://iopscience.iop.org/article/10.1149/2.F07171if.

Table of Contents Graphics